fluids

MDPI

Article

A Numerical Study of Frost Formation from Humid Air on Horizontal Cold Plate Surfaces Under Natural Convection

Zhengsheng Yang, Fan Shi *, Jiawang Li and Shukun Liu

Faculty of Maritime and Transportation, Ningbo University, Ningbo 315211, China; qz15700000525@163.com (Z.Y.); lijiawang@nbu.edu.cn (J.L.); a1820786648@163.com (S.L.)
* Correspondence: shifan@nbu.edu.cn; Tel.: +86-15824243131

Abstract

Based on a previously proposed dimensionless phase-change-driven frosting model, this study numerically investigates frost formation on a horizontal cold plate under natural convection using a Eulerian multiphase framework coupled with species transport. The model is validated against experimental data, showing errors within 5–18%; the maximum deviation of 17.07% occurs at $T_w = -25$ °C, possibly due to increased experimental uncertainty at very low temperatures. Results demonstrate that lower cold plate temperatures lead to greater frost thickness and higher ice volume fraction. A key physical insight is that under natural convection, local convective circulation causes enhanced frosting at the plate edges, resulting in spatial non-uniformity in both thickness and density. The study covers cold plate temperatures from −10 °C to −25 °C at relative humidity of 60%. The frost growth rate and density at both ends of the cold plate exceed those in the central region, and this difference intensifies with decreasing temperature. Within the frost layer, humid air velocity is nearly zero, while maximum velocity occurs near the sides due to natural convection. The simulation results show good agreement with experimental data, confirming the model's reliability for natural convection scenarios.

Keywords: frost; multi-phase flow; natural convection

1. Introduction

Frost formation is a highly complex process involving heat and mass transfer, commonly observed across various fields and often associated with significant adverse effects. Frost deposition reduces the heat transfer capacity of structural surfaces and increases flow resistance. For instance, frost on air vaporizer surfaces diminishes heat exchange efficiency [1,2], ice accretion on aircraft wings increases drag [3–5], ice accumulation on cables may lead to rupture [6,7], and icing on wind turbine blades reduces operational efficiency [8,9]. When temperatures decrease, causing the air to become supersaturated, water vapor within humid air condenses into frost. The mass transfer process between water vapor and the frost layer contributes to increases in both frost thickness and density. Over the past decades, numerous researchers have conducted experimental and simulation studies on the frost formation process.

Scholars such as Lee et al. [10] developed a frost formation model for flat plates, incorporating water molecular diffusion and water vapor sublimation within the frost layer, subsequently validating this model experimentally. Hayashi [11] investigated the growth and densification processes of frost layers on flat plate surfaces, proposing an exponential relationship between frost density and frost surface temperature. Hermes et al. [12] argued

Check for updates

Academic Editor: Kannan N. Premnath

Received: 4 February 2026
Revised: 28 February 2026
Accepted: 7 March 2026
Published: 10 March 2026

Copyright: © 2026 by the authors. Licensee MDPI, Basel, Switzerland. This article is an open access article distributed under the terms and conditions of the Creative Commons Attribution (CC BY) license.

that frost density correlates not only with the frost surface temperature but also significantly with the cold surface temperature. Based on Hermes's experimental data [12], Kandula [13] further established a non-dimension correlation relating frost density to the cold surface temperature, frost surface temperature, and the Reynolds number of humid air flow. He concluded that frost density depends primarily on these three parameters, exhibiting negligible dependence on relative humidity.

Early frost growth simulation methods neglected humid air flow, solving control equations solely for the frost layer. The model developed by Lee et al. [10]. was based on mass and energy balance within the frost layer and incorporated the supersaturation of humid air at the frost surface. Kandula [14] modified components of this model, extending its applicability to a broader range of temperature and humidity conditions.

Subsequently, Lee et al. [15] employed a dual-region approach, dividing the computational domain into humid air and frost layer regions, to model frost growth on cold surfaces. Separate control equations were established for each domain, enabling the calculation of frost height, density, and surface temperature. Building upon the framework established by Lee et al. [15]., Yang et al. [16,17] implemented refinements enabling accurate predictive capabilities for frost layer growth under turbulent flow conditions. In parallel, Na et al. [18,19] developed a novel computational approach predicated on supersaturated air at the frost interface. This model incorporates evolving frost density dynamics and employs a modified thermal conductivity correlation for frost deposition. Some previously published models that use an empirical tortuosity factor greater than 1.0 are physically unrealistic.

With advancements in computational fluid dynamics (CFD), some researchers have applied multiphase flow models to simulate frost growth. Cui et al. [20,21] proposed a Eulerian multiphase flow-based model to compute the mass transfer rate from water vapor to the ice phase, simulating frost growth on finned-tube heat exchanger surfaces. Kim et al. [22] also simulated frost growth using a Eulerian multiphase model, identifying the water vapor concentration gradient at the frost surface as the primary driving force for growth.

While previous modeling efforts have advanced the understanding of frost formation, most are tailored to forced convection conditions. One-dimensional models [10–14] cannot resolve spatial heterogeneity, and Eulerian multiphase models [20–22] often incorporate empirical correlations derived from forced convection experiments, limiting their direct applicability to natural convection. The dimensionless driving-force model proposed by Wu et al. [23] offers a more general physical basis, as it relies on local supersaturation rather than flow regime-specific assumptions. However, its empirical coefficient B was originally fitted from forced convection data, and its validity under natural convection has not been systematically examined. Therefore, this study aims to extend the Wu model to natural convection and validate its predictive capability against experimental data.

This study employs a frost formation model based on a non-dimension phase change driving force, as established by Wu et al. [23], to conduct a numerical investigation of frost formation on a horizontal cold plate under natural convection conditions. Given that previous research predominantly focused on forced convection scenarios, numerical studies under natural convection remain relatively scarce. Therefore, this study aims to integrate the Eulerian multiphase model with a species transport model to apply this phase-change-driven frost model to natural convection conditions. The study first establishes and validates the frost model by comparing simulation results with experimental and simulated data from the original source to ensure accuracy. Subsequently, the model is applied to simulate frost formation under natural convection, and the simulated results are compared with the experimental results of Song [24] concerning frost formation on horizontal cold plates under similar conditions.

The novelty of this work lies not in proposing a new model, but in validating the applicability of the Wu model under natural convection conditions, thereby extending the physical scenarios in which this model can be applied and laying the groundwork for future studies.

2. Physical Model

Figure 1 illustrates the computational domain for frost formation on a cold plate under natural convection, comprising the cold plate and the surrounding flow field region. To mitigate the influence of flow field dimensions on natural convection simulations, the length and width of the flow field are set to 200 mm and 100 mm, respectively. Additionally, we tested a flow field with dimensions of 1000 mm $\times$ 500 mm, and the measured frost layer thickness results showed an error of less than 1% compared to the results obtained from the original-sized flow field. The central cold plate measures 40 mm in length and 2 mm in width.



Figure 1. Simulation domain for frost formation on the cold plate.

A structured mesh was utilized in the simulation. Following a grid independence analysis, the ice layer thickness under the condition of $T_w = -10$ °C was found to be 846×10^{-6} m, 872×10^{-6} m, 901×10^{-6} m, and 906×10^{-6} m for mesh counts of 100 k, 370 k, 550 k, and 820 k, respectively.

The relative error between the 550 k grid and the 820 k grid is only 0.55 %(Figure 2), indicating that the changes resulting from further refinement are negligible. To balance accuracy and computational cost, the 550 k grid was selected, and boundary layer refinement was performed near the wall surface (Figure 3).

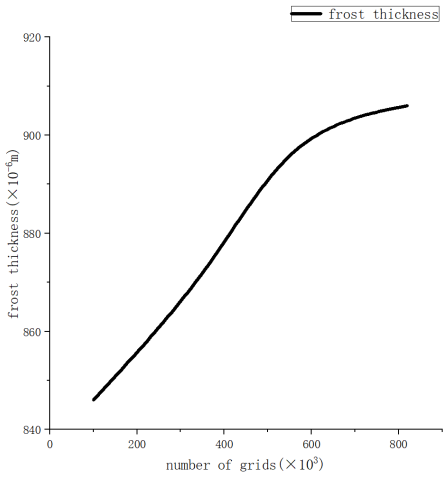


Figure 2. Grid independence test.

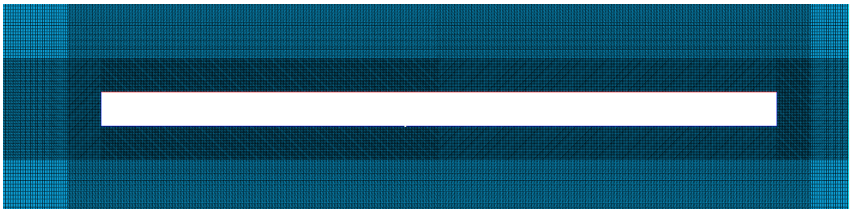


Figure 3. Mesh generation of the simulation domain.

3. Mathematic Model and Numerical Method

The frost formation process is highly complex, and various mathematical models exist. This study adopts a frost model proposed by Wu Xiaomin, Zhu Fuqiang, and colleagues [23]. Frost growth occurs as mass, momentum, and energy are transferred from water vapor in the humid air phase to the ice phase.

3.1. Governing Equations

The simulation employs the Eulerian multiphase approach. Since ice forms solely via the sublimation of water vapor, other phase changes are neglected. The primary phase is defined as humid air, and the secondary phase is ice. The volume fraction represents the content of each phase.

$$\alpha_{\mathrm{a}} + \alpha_i = 1 \tag{1}$$

where α_{a} is the volume fraction of humid air and α_i is the volume fraction of ice.

3.2. Mass Transfer Model

3.2.1. Phase Change Mass Transfer Rate

When humid air is supersaturated and the temperature within a control volume is below 0 °C, water vapor transfers from the humid air phase to the ice phase. The system's chemical potential decreases as humid air transitions from supersaturated to saturated states via vapor sublimation. The phase change driving force for frost formation equals the reduction in Gibbs free energy when water molecules transfer from the vapor to the solid state.

$$-\Delta g = k \cdot T \cdot \ln \frac{p_v}{p_{vs}} \tag{2}$$

where k is the Boltzmann constant, T is the control volume temperature, p_v is the partial pressure of water vapor in the humid air, and p_{vs} is the saturation pressure of water vapor at temperature T. Due to the typically low supersaturation in frost formation, the values of p_v and p_{vs} are very close, Equation (2) can be approximated as:

$$-\Delta g = k \cdot T \cdot \frac{p_v - p_{vs}}{p_{vs}} \tag{3}$$

The water vapor partial pressure relates to its mass fraction in humid air.

$$w_v = 0.622 \frac{p_v}{p^0} \tag{4}$$

where p^0 is atmospheric pressure. Combining Equations (3) and (4), the phase change driving force is proportional to

$$-\Delta g \propto k \cdot T \cdot \frac{w_v - w_{vs}}{w_{vs}} \tag{5}$$

where w_{vs} is the saturated water vapor mass fraction at temperature T. The expression $\frac{w_v - w_{vs}}{w_{vs}}$ can represent the non-dimension phase change driving force for frost formation.

The mass transfer rate $\dot{m}_{ai}$ depends on this driving force and the effective density of water vapor. It is calculated as

$$\dot{m}_{\mathrm{a}i} = \tau_v \alpha_{\mathrm{a}} \rho_{\mathrm{a}} w_v \frac{w_v - w_{vs}}{w_{vs}} \tag{6}$$

where τ_v is the time relaxation coefficient. This coefficient correlates with the Reynolds number and is defined by an empirical relationship derived from regression analysis of analytical data.

$$\tau_v = 16.705 + 0.000352\ \mathrm{Re}^{1.684} \tag{7}$$

3.2.2. Frost Growth and Densification Criterion

During frost formation, both frost thickness and density increase over time: phase change at the frost surface increases thickness, while phase change within the frost layer due to vapor diffusion increases density, as illustrated in Figure 4.

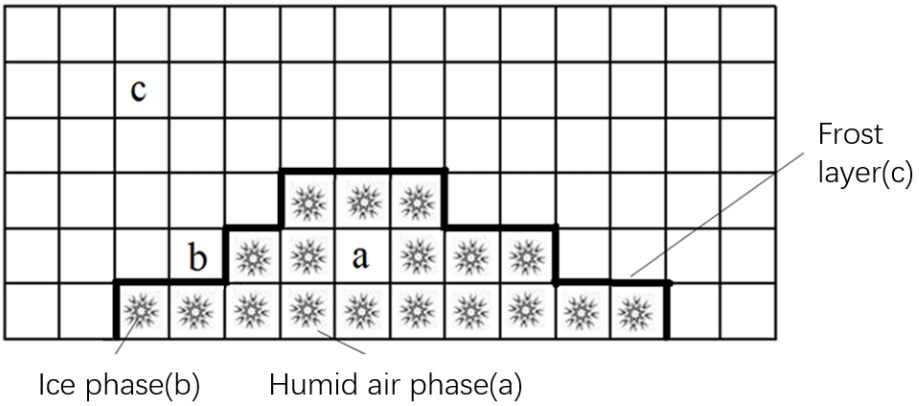


Figure 4. Schematic diagram of frost growth region division.

Based on previous work [25], a phase change mass transfer criterion is established using a non-dimension coefficient B, the non-dimension driving force, and a non-dimension humid air velocity to describe the frost growth and densification processes.

$$\dot{m}_{\mathrm{a}i} = \begin{cases} \tau_v \alpha_{\mathrm{a}} \rho_{\mathrm{a}} w_v \frac{w_v - w_{vs}}{w_{vs}} & \frac{w_v - w_{vs}}{w_{vs}} \geq B \cdot \frac{u_a}{u_{in}} \\ 0 & \frac{w_v - w_{vs}}{w_{vs}} < B \cdot \frac{u_a}{u_{in}} \end{cases} \tag{8}$$

The non-dimension coefficient B characterizes frost thickness growth. The correlation for B, shown below, was obtained by fitting simulated frost thickness values against experimental data.

$$B = \left(-4.8T_w^2 + 2489T_w - 3.21 \times 10^5\right) \cdot (-0.687u_{in} + 1.771) \cdot w_{in} \tag{9}$$

Within the frost layer region, the humid air flow velocity is approximately zero, and water vapor enters the frost layer through diffusion. Under this condition, the relationship $\frac{w_v - w_{vs}}{w_{vs}} > B \cdot \frac{u_a}{u_{in}}$ is satisfied. Therefore, the phase change mass transfer process from water vapor to the ice phase leads to an increase in frost density. At the frost surface region, the air velocity at the bottom of the humid air flow velocity boundary layer is sufficiently small. At the bottom of the velocity boundary layer, the relationship $\frac{w_v - w_{vs}}{w_{vs}} \geq B \cdot \frac{u_a}{u_{in}}$ is satisfied, and ice crystals formed by phase change deposit onto the frost surface, resulting in an increase in frost thickness. Furthermore, when the non-dimension phase change driving force $\frac{w_v - w_{vs}}{w_{vs}}$ increases, the phase change region at the bottom of the velocity boundary layer expands, which signifies an acceleration in the frost layer growth rate. In the humid air flow region, the air velocity is relatively high and satisfies the relationship $\frac{w_v - w_{vs}}{w_{vs}} < B \cdot \frac{u_a}{u_{in}}$.

Consequently, the mass transfer rate $\dot{m}_{ai}$ equals zero, indicating that no frost formation phenomenon occurs.

3.3. Interphase Momentum Transfer

The momentum exchange coefficient K between the two phases is given by:

$$K = \frac{18\rho_a \alpha_a v_a \alpha_i f}{d_i^2} \tag{10}$$

where f is the drag coefficient. The drag function is provided by the Wen-Yu's correlation:

$$f = (1 + 0.15\,\mathrm{Re}_i^{0.687}) \cdot \alpha_a^{-2.65} \tag{11}$$

3.4. Interphase Energy Transfer

The intensity of heat exchange between the phases satisfies the local equilibrium condition $Q_{ia} = -Q_{ai}$. The heat exchange rate relates to the temperature difference between the phases.

$$Q_{ia} = h_{ia}(T_i = T)_a \tag{12}$$

where h_{ia} is the interphase heat transfer coefficient, calculated as

$$h_{ia} = \frac{6\lambda_a \alpha_i \alpha_a Nu_{ia}}{d_i^2} \tag{13}$$

where λ_a is the thermal conductivity of humid air. The Nusselt number Nu_{ia} is given by the Ranz-Marshall correlation:

$$Nu_{ia} = 2.0 + 0.6\,\mathrm{Re}_i^{1/2}\,\mathrm{Pr}_a^{1/3} \tag{14}$$

3.5. Boundary Conditions

Due to the room being large enough for the cold plate, the computational domain represents an open environment. Therefore, the outer boundary is defined as the pressure inlet condition to maintain environmental pressure and temperature. All walls are set to non-slip boundaries. Apply a constant temperature to the surface of the cold plate according to the operating conditions listed in Table 1. The other walls are assumed to be adiabatic. A Eulerian multiphase flow model was employed for the calculation, configured with two phases: humid air and ice. Since the water vapor concentration was very low, the thermal conductivity of the primary phase was assumed to be the value for dry air. Other physical property parameters for the primary phase were calculated as the weighted averages of the dry air and water-vapor properties given in the FLUENT database. The corresponding thermophysical properties are listed in Table 2. The humid air phase comprises dry air and water vapor, and the mass fractions of these components were specified at the humid air inlet boundary. Interphase mass transfer and interphase forces were incorporated into the simulation via user-defined functions. Since the simulation pertains to natural convection, the density was specified according to the ideal gas law.

Table 1. Five specific simulation cases.

Case	T_{cp} (°C)	RH (%)	T_a (°C)
1	−10	60	23
2	−15	60	23
3	−20	60	23
4	−25	60	23

Table 2. Thermophysical properties of humid air and ice.

Substance	Density kg/m^3	Thermal Conductivity W/(m·K)	Specific Heat J/(kg·K)	Coefficient of Viscosity kg/(m·s)
Dry air	1.225	-	-	1.79×10^{-5}
Water-vapor	0.554	-	-	1.34×10^{-5}
Humid air	ideal gas	0.024	1006.4	mass-weighted
Ice	915	2.5	2100	-

The simulation cases are detailed in Table 1.

4. Results

4.1. Model Validation

The model validation is based on the channel flat plate frost experiments conducted by Wu, Chu et al. [23]. The geometric model dimensions H_y, L_{x1}, L_{x2} are 5 mm, 25 mm, and 50 mm, respectively, as shown in Figure 5.

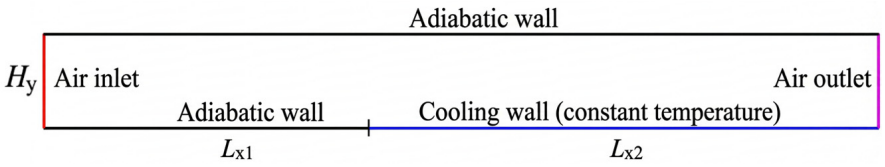


Figure 5. Geometric model of the frost experiment.

The simulation results obtained during the validation process, as shown in Figure 6, demonstrate high consistency with both the experimental data and simulation results reported by Wu [23]. Thus, the validity of the model is confirmed.

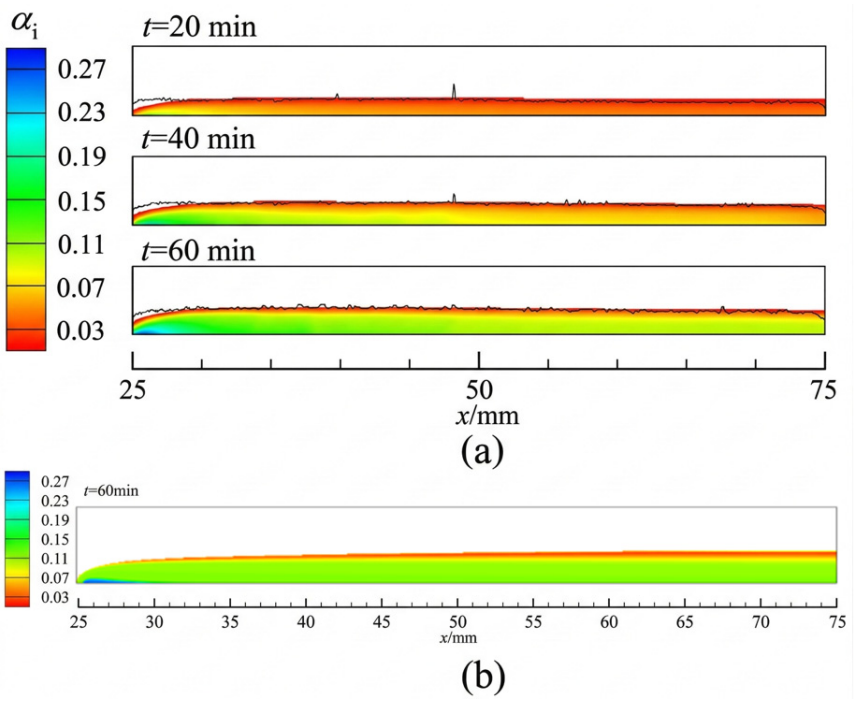


Figure 6. Ice volume fraction distribution ($T_w = -13$ °C, $T_a = 2$ °C. RH = 85%, $u_{in} = 0.92$ m/s): (**a**) Simulation results of WU, (**b**) Model validation results.

4.2. Analysis of Experimental Results

In order to illustrate the variation in frost thickness under different surface temperatures over the entire 1200 s period, Song et al. captured photographs at six time points

during the experiment—specifically at 200 s, 400 s, 600 s, 800 s, 1000 s, and 1200 s—as shown in Figure 7. In Figure 7(4a), the white area represents the frost layer. It can be observed that the frost thickness increases with frosting time. For example, Figure 7(3a–3e), the frost thickness grows from about one-quarter to one-half of the field of view.

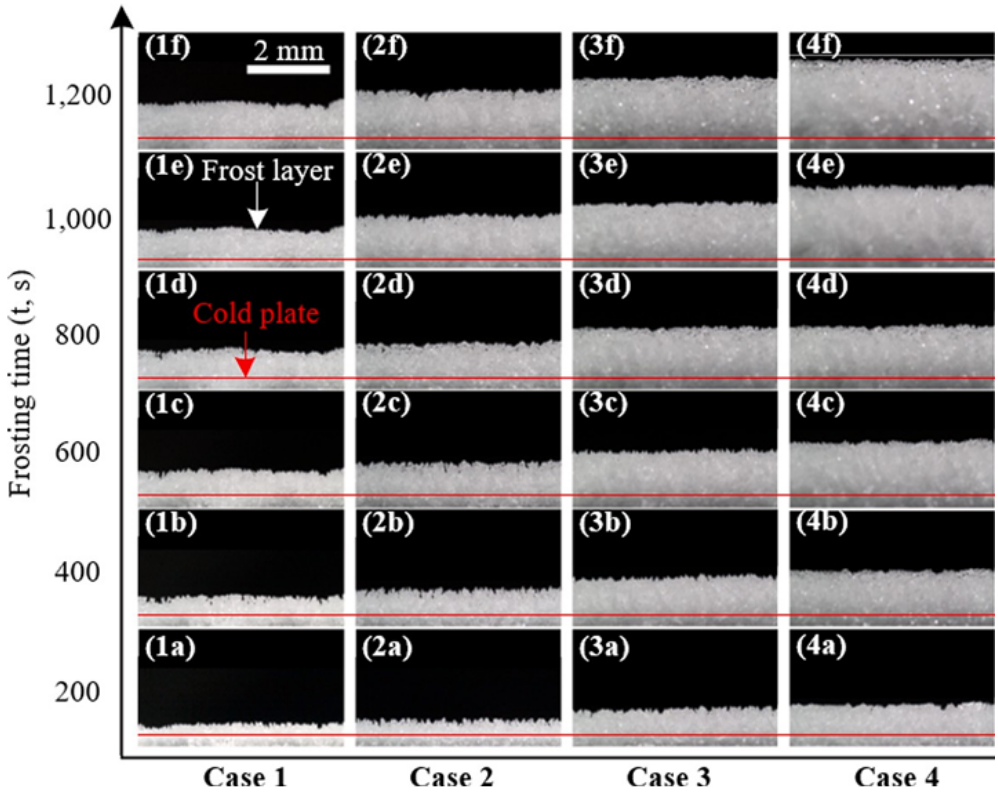


Figure 7. Frost formation on the surface of the cold plate at different times under four different conditions.

A lower surface temperature results in more frost accumulation on the cold plate surface. For instance, in Figure 7(1b), taken 400 s after the onset of frosting, the frost layer coverage is close to 20%, while in Figure 7(4b), the coverage is approximately 50%. Furthermore, at each time point, the increase in frost thickness becomes more pronounced as the surface temperature decreases. In Case 1, Figure 7(1a–1f), the frost thickness increases from 10% to 40%, representing an increase of about 30% of the field of view. In Case 5, Figure 7(4a–4f), the frost thickness rises from 35% to 85%, corresponding to an increase of approximately 50% of the field of view. The frost layer thickness experimentally measured at 600 s and 1200 s are presented in Table 3.

Table 3. Frost layer thickness at 600 s and 1200 s for the four cases.

	−10 °C	−15 °C	−20 °C	−25 °C
600 s frost layer thickness $(10^{-6}$ m)	544	764	981	1249
1200 s frost layer thickness $(10^{-6}$ m)	830	1113	1332	1797

4.3. Frost Distribution on Cold Plates at Different Temperatures

Frost thickness is one of the key parameters reflecting the influence of cold plate temperature on the frosting process. This study simulated the evolution of frost thickness from 600 s to 1200 s under four cold plate temperatures: −10 °C, −15 °C, −20 °C, and −25 °C. Figure 8 illustrates the simulated frost thickness at 200 s intervals. A comparison

of frost thickness between the simulation results and experimental data is presented in Figure 9.

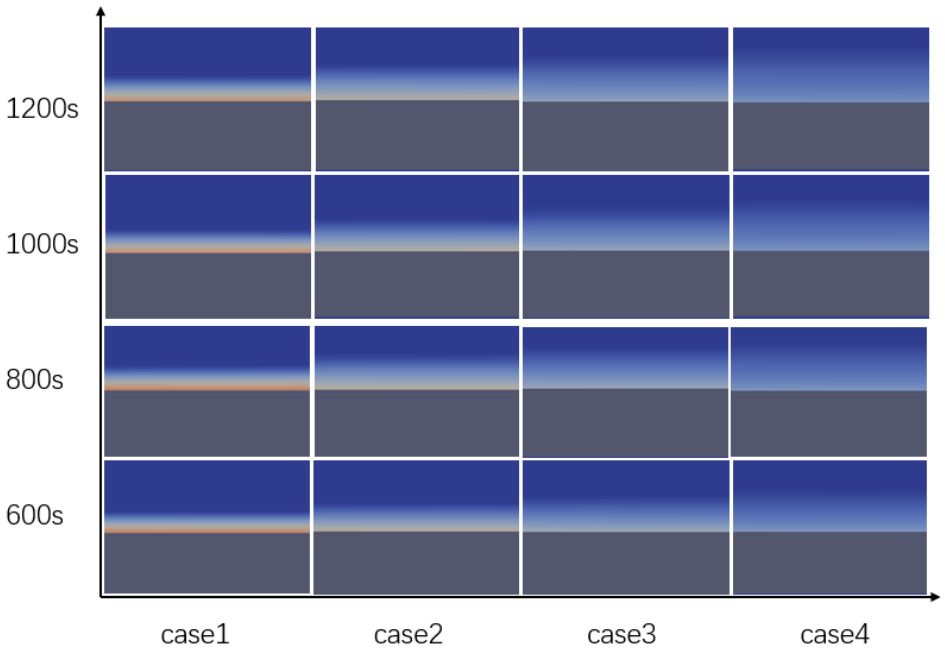


Figure 8. Contour plots of frost thickness at different stages.

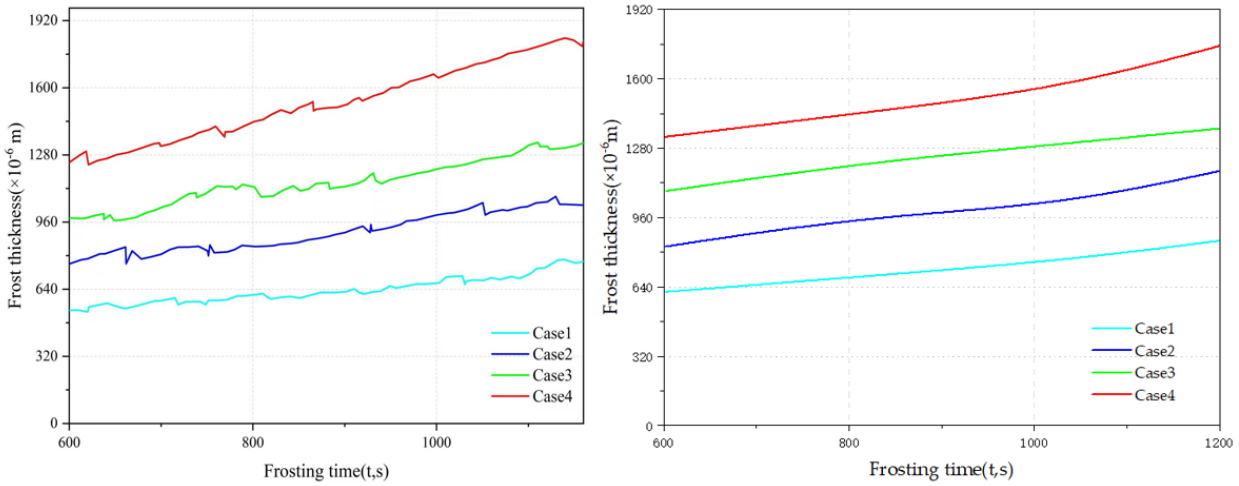


Figure 9. Time-dependent quantitative values of frost thickness: (**a**) experiment; (**b**) simulation.

Frost thickness stands as one of the primary factors reflecting the influence of cold plate temperature on the frost formation process. Figure 9 illustrates the frost growth and ice volume fraction under four different cold plate temperatures with the time pass. As depicted in Figure 9, under test conditions of T_w= −10 °C, −15 °C, −20 °C, and −25 °C, the corresponding frost thicknesses on the cold plate are 901 × 10^{-6}m, 1303 × 10^{-6}m, 1484 × 10^{-6}m, and 1902 × 10^{-6}m, respectively, with the maximum thickness occurring near the center of the cold plate. According to Figure 10, the experimental errors are controlled within 18%, with the maximum error being 17.07% and the minimum error as low as −6.32%.

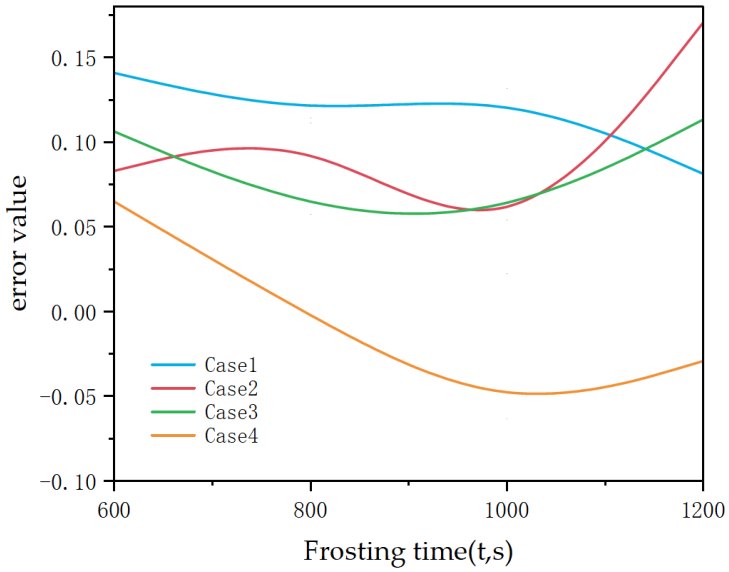


Figure 10. Error value between experimental results and simulation results.

As shown in Figure 10, the maximum relative error in frost thickness reaches 17.07% at $T_w = -15$ °C. This phenomenon may be attributed to two main factors. First, experimental observations by Song et al. suggest inherent uncertainties, as the complex morphology of the frost surface increases the difficulty of accurate interface identification, leading to higher uncertainty in the experimental data itself. Second, the empirical coefficient B in Wu's model was originally fitted from experimental data and thus has inherent limitations in accuracy and applicability under natural convection; the −15 °C condition may lie in a regime where the coefficient B is particularly sensitive to variations in flow conditions, thereby amplifying the simulation deviation. Despite this local deviation, the overall trend shows good agreement between simulation results and experimental data, with errors generally within a reasonable range, demonstrating that the model possesses satisfactory overall predictive capability.

Under simulated natural convection conditions, the temperature within the chamber remains constant, while a temperature decrease is observed near the cold plate. In high humidity environments, the partial pressure of water vapor is relatively high, and the sublimation rate is limited, so the deviation of surface temperature from 0 °C is very small. For the convenience of measurement, we use a 0 °C isotherm to approximate and simplify the frost layer surface line, which helps to compare the measurement of frost layer thickness with experimental observations. As illustrated in Figure 11, the 0 °C isotherm corresponds to the frost layer surface.

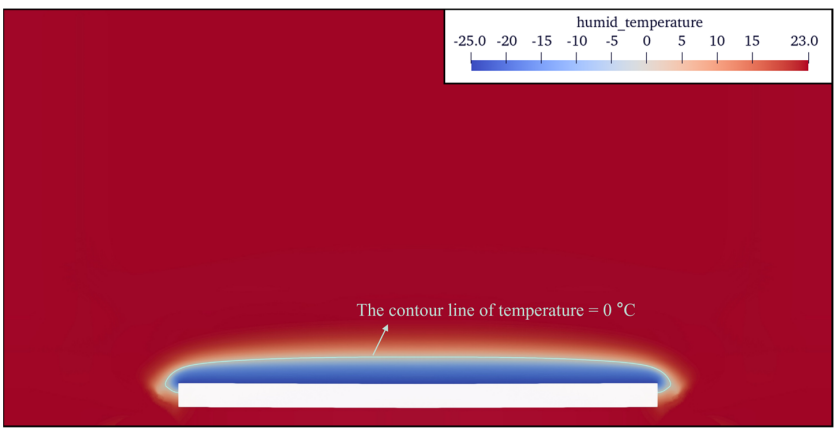


Figure 11. Temperature distribution contour of humid air.

4.4. Ice Volume Fraction Distribution

The frost layer is regarded as a porous medium composed of moist air and ice; therefore, it is represented in Figure 10 using the contour of ice volume fraction in the ice phase. The region from x = 80 mm to x = 120 mm corresponds to the cold plate section. Under natural convection conditions, the frost distribution exhibits symmetry about x = 100 mm. Hence, only the frost layer distribution from x = 80 mm to x = 100 mm is presented in this study.

As can be observed in Figure 12, at t = 1200 s, a decrease in the cold plate temperature not only leads to an increase in frost thickness but also raises the ice volume fraction across various locations within the frost layer, indicating a densification of the structure. Higher ice volume fractions and greater frost accumulation are observed near both ends of the cold plate, whereas the central region exhibits relatively uniform frost deposition. In natural convection, the temperature difference induces air motion, resulting in higher airflow velocities near the edges of the cold plate. This enhanced convective effect accelerates frost formation in these areas, leading to a higher local ice volume fraction.

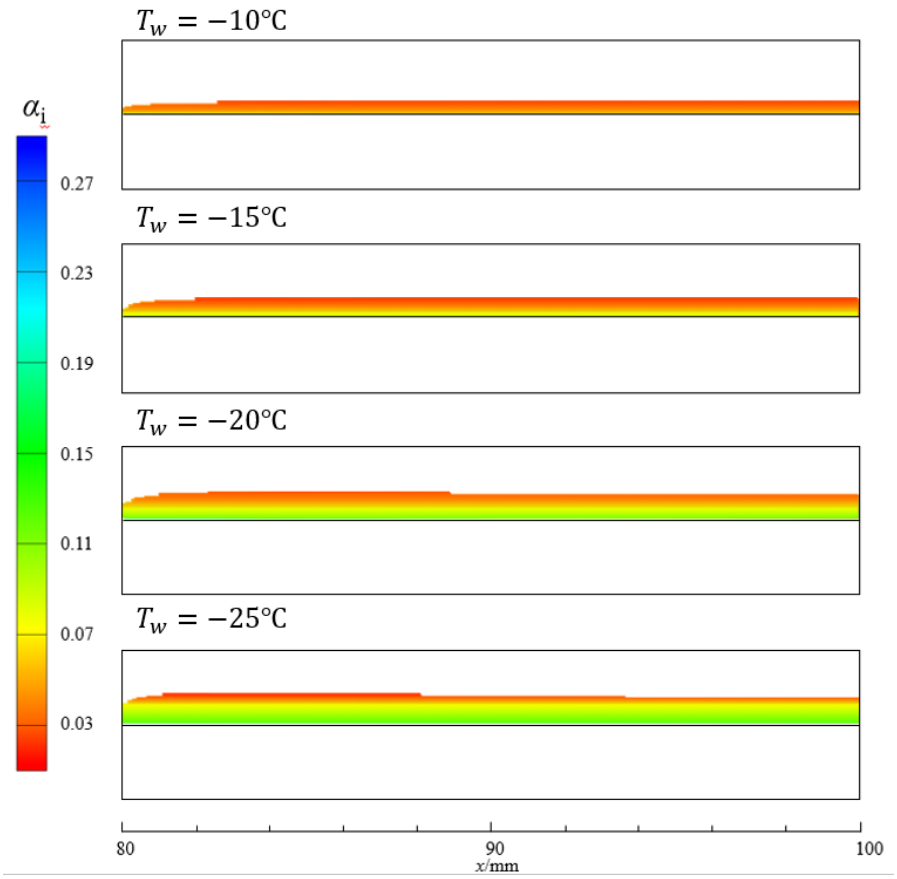


Figure 12. Ice volume fraction distribution on cold plates at different temperatures at 1200 s.

Figure 13 shows the distribution of ice volume fraction at five different x-coordinate positions (x = 30 mm, 40 mm, 50 mm, 60 mm, and 70 mm) at y = 0.01 mm (where y = 0 is defined as the upper edge of the cold plate), under the conditions of RH = 60% and T_a = 23 °C, for different cold plate temperatures. It can be observed that as the cold plate temperature decreases, the ice volume fraction at the same location increases, indicating a higher frost density. At T_w = −10 °C, due to the relatively high cold plate temperature, the frost layer is thin, and the frost density is low with relatively uniform density throughout. As the cold plate temperature decreases further, the difference in ice volume fraction between the ends and the middle becomes significantly larger, and the difference in frost

density becomes notable. It can be concluded that the lower the cold plate temperature, the greater the difference in frost density and frosting rate between the ends and the middle.

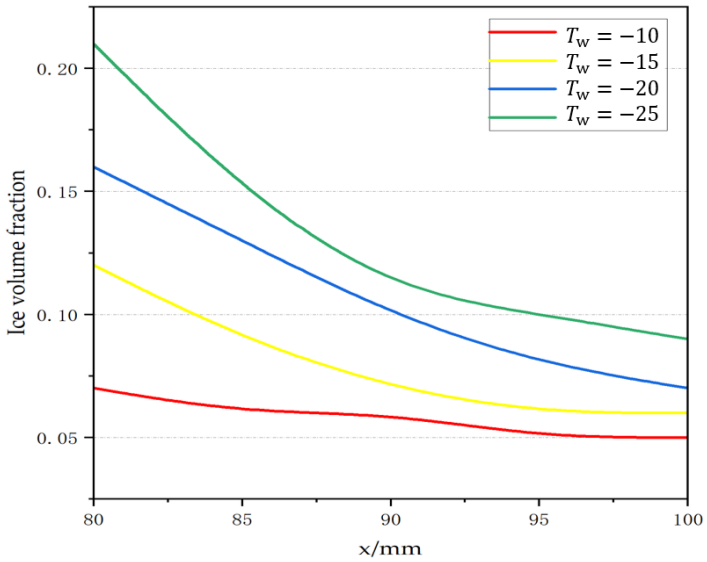


Figure 13. Variation in ice volume fraction with temperature at different locations.

4.5. Velocity Distribution

In order to quantitatively characterize the natural convection state, we calculated the Rayleigh numbers for four operating conditions, Ra = 2.58×10^5, 3.11×10^5, 3.70×10^5, 4.35×10^5. It was confirmed that the flow under all studied conditions was in laminar flow.

Figure 14 presents the velocity contour of the humid air phase at $T_w = -10$ °C. It can be observed that the flow velocity reaches its maximum at both ends of the cold plate. When $T_w = -10$ °C, −15 °C, −20 °C, and −25 °C, the maximum velocities are 1.27 m/s, 1.28 m/s, 1.30 m/s, and 1.31 m/s, respectively. Due to the established temperature difference of 34 °C, the magnitude of the air velocity does not change significantly as the cold plate temperature decreases. Because the humid air flow velocity is high in these regions, the heat and mass transfer efficiency is highest here, which in turn leads to the fastest frost deposition rate at both ends of the cold plate.

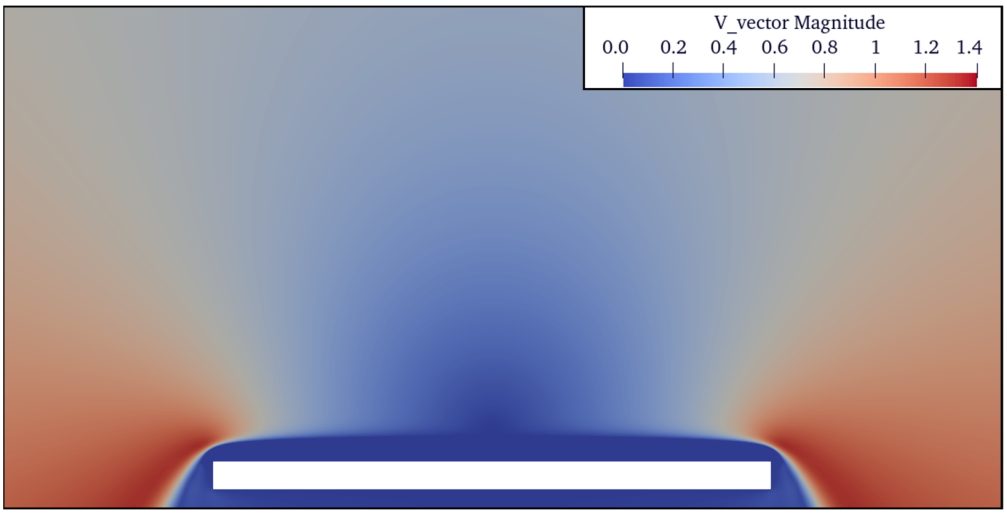


Figure 14. Velocity distribution contour of humid air.

As shown in the velocity vector plot in Figure 15, the density of the humid air above the central region of the cold plate increases due to natural convection, causing the air to

descend and flow outward from the edges of the cold plate, thereby generating a convective circulation effect.

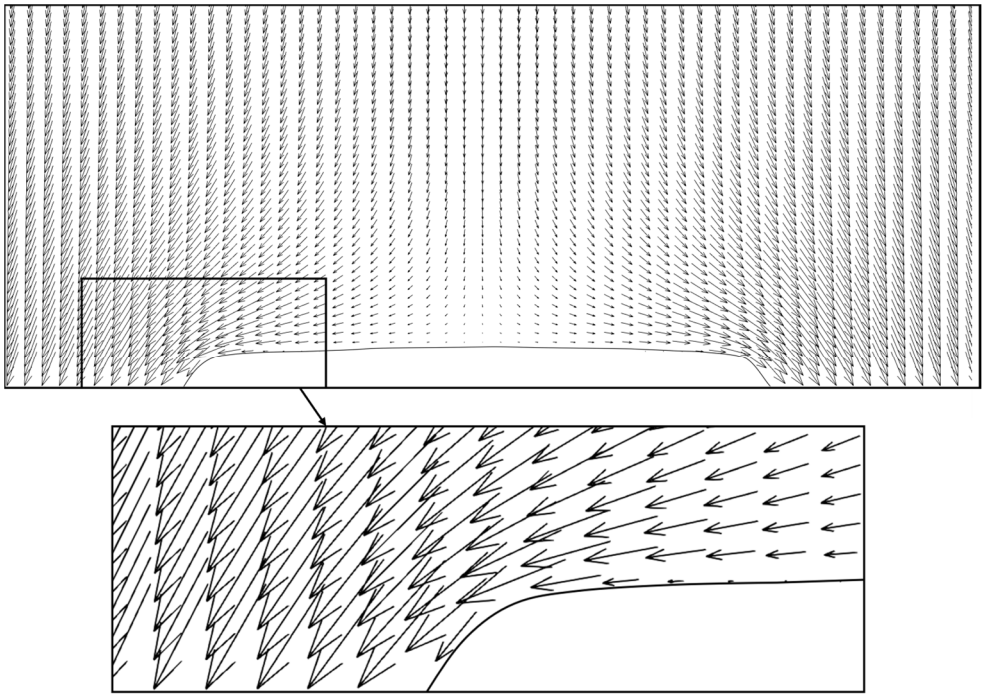


Figure 15. Velocity vector plot of humid air.

5. Conclusions

This study employed a multiphase flow model to simulate the frost formation process on the upper surface of a cold plate under natural convection conditions. The simulated frost growth and densification processes show good agreement with experimental results. The model accurately predicted the frost layer thickness, with deviations ranging from 5% to 18% compared to experimental measurements, thereby validating its reliability for natural convection scenarios. It should be noted that the validation scope of this study is limited to the specific conditions of natural convection scenarios used in this study. Extrapolation of significantly different parameters should be handled with caution, and it is recommended to use additional experimental data for further validation.

Based on the simulation results, the following conclusions can be drawn:

1. Under natural convection conditions, lower cold plate temperatures result in greater frost layer thickness and higher ice volume fractions across all spatial positions.
2. Under natural convection conditions, the frost density reaches its maximum at both ends of the cold plate. The frost deposition rate at the edges exceeds that at the central region, and this differential exhibits significant enhancement with decreasing temperature.
3. Within the frost layer region, the humid air velocity approaches zero. In the humid air region, however, the maximum flow velocity occurs at both sides of the cold plate due to convective effects.

This study demonstrates that a phase-change-driven frosting model originally developed for forced convection can be successfully extended to natural convection. Under natural convection conditions, frost growth is non-uniform: due to local convective circulation, enhanced frosting occurs at the edges of the cold plate, resulting in greater thickness and density. This spatial heterogeneity has practical implications: anti-frosting strategies should prioritize edge regions, and performance predictions for natural-convection-dominated

equipment should account for this non-uniformity. The validated model provides a useful tool for predicting frost formation under natural convection within the studied range.

Author Contributions: Conceptualization, Z.Y.; Methodology, F.S.; Software, Z.Y.; Validation, Z.Y.; Formal analysis, Z.Y.; Investigation, Z.Y.; Resources, F.S. and J.L.; Writing—original draft, Z.Y.; Writing—review and editing, Z.Y.; Visualization, Z.Y.; Supervision, F.S., J.L. and S.L.; Project administration, F.S.; Funding acquisition, F.S. and J.L. All authors have read and agreed to the published version of the manuscript.

Funding: This research received no external funding.

Institutional Review Board Statement: Not applicable.

Informed Consent Statement: Not applicable.

Data Availability Statement: The original contributions presented in this study are included in the article material. Further inquiries can be directed to the corresponding author(s).

Conflicts of Interest: The authors declare no conflict of interest.

References

1. Kuang, Y.W.; Yi, C.C.; Wang, W. Numerical simulation of frosting behavior and its effect on a direct-contact ambient air vaporizer. *J. Nat. Gas Sci. Eng.* **2015**, *27*, 55–63. [CrossRef]
2. Jadav, C.; Chowdhury, K. Minimizing weight of ambient air vaporizer by using identical and different number of fins along the length. *J. Renew. Energy* **2021**, *163*, 398–413. [CrossRef]
3. Wu, Z.; Cao, Y.H. Airfoil performance degradation by coupling effects of supercooled raindrop icing and heavy rainfall. *J. Proc. Inst. Mech. Eng. Part G. J. Aerosp. Eng.* **2017**, *231*, 2384–2395. [CrossRef]
4. Akgun, O.; Kalayci Doner, N. Anti-icing and de-icing methods used for icing at wings of aircrafts. *J. Polytech.* **2024**. [CrossRef]
5. Potapczuk, M.G. Aircraft Icing Research at NASA Glenn Research Center. *J. Aerosp. Eng.* **2013**, *26*, 260–276. [CrossRef]
6. Zhang, W.; Li, M.Y.; Wu, Q.L.; Xi, A. Nonlinear vibration of iced cable under wind excitation using three-degree-of-freedom model. *J. Chin. Phys. B* **2021**, *30*, 090503. [CrossRef]
7. Wagner, T.; Peil, U. Ice accretion on cables. *Stahlbau* **2009**, *78*, 841–848. [CrossRef]
8. Madi, E.; Pope, K.; Huang, W.M.; Iqbal, T. A review of integrating ice detection and mitigation for wind turbine blades. *Renew. Sustain. Energy Rev.* **2019**, *103*, 269–281. [CrossRef]
9. Jin, J.Y.; Virk, M.S.; Hu, Q.; Jiang, X.L. Study of ice accretion on horizontal axis wind turbine blade using 2D and 3D numerical approach. *IEEE Access* **2020**, *8*, 166236–166245. [CrossRef]
10. Lee, K.; Lee, T.; Kim, W. A one-dimensional model for frost formation on a cold flat surface. *Int. J. Heat Mass Transf.* **1997**, *40*, 4359–4365. [CrossRef]
11. Hayashi, Y.; Aoki, A.; Adashi, S. Study of frost properties correlating with frost formation types. *ASME J. Heat Transf.* **1977**, *99*, 239–245. [CrossRef]
12. Hermes, C.J.L.; Piucco, R.O.; Barbosa, J.R. A study of frost growth and densification on flat surfaces. *Exp. Therm. Fluid Sci.* **2009**, *33*, 371–379. [CrossRef]
13. Kandula, M. Correlation of water frost porosity in laminar flow over flat surfaces. *Spec. Top. Rev. Porous Media Int. J.* **2012**, *3*, 79–87. [CrossRef]
14. Kandula, M. Frost growth and densification in laminar flow over flat surfaces. *Int. J. Heat Mass Transf.* **2011**, *54*, 3719–3731. [CrossRef]
15. Lee, K.; Jhee, S.; Yang, D. Prediction of the frost formation on a cold flat surface. *Int. J. Heat Mass Transf.* **2003**, *46*, 3789–3796. [CrossRef]
16. Yang, D.K.; Lee, K.S. Modeling of frosting behavior on a cold plate. *Int. J. Refrig.* **2005**, *28*, 396–402. [CrossRef]
17. Yang, D.K.; Lee, K.S.; Cha, D.J. Frost formation on a cold surface under turbulent flow. *Int. J. Refrig.* **2006**, *29*, 164–169. [CrossRef]
18. Na, B.C.; Webb, R.L. New model for frost growth rate. *Int. J. Heat Mass Transf.* **2004**, *47*, 925–936. [CrossRef]
19. Na, B.C.; Webb, R.L. Mass transfer on and within a frost layer. *Int. J. Heat Mass Transf.* **2004**, *47*, 899–911. [CrossRef]
20. Cui, J.; Li, W.Z.; Liu, Y.; Zhao, Y.S. A new model for predicting performance of fin-and-tube heat exchanger under frost condition. *Int. J. Heat Fluid Flow* **2011**, *32*, 249–260. [CrossRef]
21. Cui, J.; Li, W.Z.; Liu, Y.; Jiang, Z.Y. A new time- and space-dependent model for predicting frost formation. *Appl. Therm. Eng.* **2011**, *31*, 447–457. [CrossRef]

22. Kim, D.; Kim, C.; Lee, K.-S. Frosting model for predicting macroscopic and local frost behaviors on a cold plate. *Int. J. Heat Mass Transf.* **2015**, *82*, 135–142. [CrossRef]
23. Wu, X.M.; Chu, F.Q.; Ma, Q. Frosting model based on phase change driving force. *Int. J. Heat Mass Transf.* **2017**, *110*, 760–767. [CrossRef]
24. Song, M.J.; Shangwen, L.; Hosseini, S.H.; Luo, X.Y.; Wang, Z.H. An experimental study on the effect of horizontal cold plate surface temperature on frosting characteristics under natural convection. *Appl. Therm. Eng.* **2022**, *211*, 118416. [CrossRef]
25. Wu, X.M.; Ma, Q.; Chu, F.Q.; Hu, S. Phase change mass transfer model for frost growth and densification. *Int. J. Heat Mass Transf.* **2016**, *96*, 11–19. [CrossRef]

Disclaimer/Publisher's Note: The statements, opinions and data contained in all publications are solely those of the individual author(s) and contributor(s) and not of MDPI and/or the editor(s). MDPI and/or the editor(s) disclaim responsibility for any injury to people or property resulting from any ideas, methods, instructions or products referred to in the content.